IEEE Access
Multidisciplinary | Rapid Review | Open Access Journal

Received 4 August 2024, accepted 28 August 2024, date of publication 5 September 2024, date of current version 13 September 2024.

Digital Object Identifier 10.1109/ACCESS.2024.3454692

RESEARCH ARTICLE

Automatized End Mill Wear Inspection Using a Novel Illumination Unit and Convolutional Neural Network

MÜHENAD BILAL[1], RANADHEER PODISHETTI[1], LEONID KOVAL[1], MAHMOUD A. GAAFAR[2,3], DANIEL GROSSMANN[1], AND MARKUS BREGULLA[1]

[1]Application Cluster "Digital Production" Progarm, AImotion Bavaria Instiutute, Technische Hochschule Ingolstadt, 85049 Ingolstadt, Germany
[2]Department of Physics, Faculty of Science, Menoufia University, Menoufia 32952, Egypt
[3]Institute of Optical and Electronic Materials, Hamburg University of Technology, 21073 Hamburg, Germany

Corresponding author: Mühenad Bilal (muehenad.bilal@thi.de)

This work was supported in part by the Research and Development Program "Forschung und Entwicklung (FUE) Programm Informations—und Kommunikationstechnik Bayern" of the Free State of Bavaria under Grant IUK578/001 and Grant IUK578/002, and in part by the Open Access Publication Fund of Technische Hochschule Ingolstadt (THI).

ABSTRACT Ensuring cutting tools are in optimal condition is essential for achieving peak machining performance, given their direct impact on both workpiece quality and process efficiency. However, accurately assessing wear on end mills, especially those with complex geometries, pose a significant challenge due to their reflective surfaces and varied wear patterns. Presented here is a novel method that addresses this challenge by employing a customized illumination unit in conjunction with a convolutional neural network (CNN) for end mill wear analysis. This innovative approach involves utilizing the specially designed illumination unit to capture high-quality images, enabling precise examination of material wear on helically shaped end mills. Notably, this method is tailored to illuminate reflective surfaces and represents a pioneering application in the realm of wear testing.We validate the viability of this approach by employing CNN-based models to segment wear on complex-shaped end mills coated with titanium carbonitride (TiCN) and titanium nitride (TiN). We achieved remarkable mean Intersection over Union (mIoU) results in wear detection on a test dataset: 0.99 for tool segmentation, 0.78 for abnormal wear, and 0.71 for normal wear segmentation.

INDEX TERMS Cutting tools, machining performance, end mills, wear analysis, convolutional neural network, illumination source, reflective surfaces, material wear, helical geometries, wear segmentation.

I. INTRODUCTION

Examining the condition of cutting tools is critical for maintaining and improving the quality of a milling machine's production. Wear and damage to these tools can directly affect the surface quality of the workpiece and the efficiency of the machining process. Tool wear accounts for 20-30% of the total downtime of a milling machine [1], [2] and tool changes make up 3-12% of the overall machining costs [3]. Consequently, the evaluation of tool quality and wear has received considerable attention in the machining industry.

The associate editor coordinating the review of this manuscript and approving it for publication was Alba Amato.

Despite considerable recent advances in cutting tools, tool wear inspection remains a major challenge in Computer Numerical Control (CNC) manufacturing, particularly due to the complexity of accurately assessing the wear on tools with complex geometrical structures. During the machining process, the cutting tool is subjected to various simultaneous mechanical and thermal stresses, leading to different types of wear. The primary causes of tool wear include mechanical abrasion, shearing off pressure welds, oxidation, and diffusion. Tool wear can bee classified into two main categories: normal and abnormal wear. Normal wear is a natural consequence of machining, influenced by factors such as cutting parameters, tool material, and

workpiece material [4], [5], [6]. However, abnormal wear owing to adverse factors such as excessive cutting forces, poor lubrication, material adhesion, or outright tool failure.

Abnormal wear, often coupled with excessive cutting forces, can lead to a cascade of further abnormal wear incidents. To prevent or minimize the occurrence of abnormal wear, a thorough examination of, both pre- and post-machining cutting tools, is essential. Such examinations assist in optimizing the design of tools by considering their technical parameters to enhance their resilience against the forces and stresses encountered during machining. Therefore, there is considerable demand for a milling tool inspection system that can effectively characterize different types of tool wear. Currently, there are two categories of tool failure detection technologies: indirect and direct methods. Indirect methods analyze various signals generated under different cutting conditions, such as acoustic emission [6], [7], temperature variation [8], strain, vibration signals [9], motor current, power of spindle with a neural network technique [10], and cutting forces [11]. However, these methods require a significant number of high-performance sensors to be installed at specified locations on the machining equipment, which increases the machining costs and poses obstacles in the working spaces. In contrast, the direct method can be considered more cost-effective. These methods predominantly involve the implementation of machine vision techniques to assess various forms of tool failure. By utilizing cameras, microscopes, scanners, and image processing techniques normal and abnormal wear can be identified. Machine vision techniques have proven to be effective in investigating tool failures by analyzing tool wear, workpiece surface quality and chip morphology [11], [12]. In this regard, Wang et al. investigated the normal and abnormal wear of various inserts of rotary milling cutters using a coarse-to-fine strategy and a threshold-independent edge detection method [14], [15]. Although camera-based machine vision methods provide better inspection in terms of time, cost-effectiveness and flexibility, they are sensitive to cutting fluids, lighting conditions and chips, and therefore require downtime for measurement [16].

A CNN-based wear detection approach using a convolutional autoencoder (CAE) is introduced in [18], [19], and [20]. High-resolution images from optical microscopy were used for tool wear labeling and inspection, but the method is limited to small tool regions due to the microscope's field of view. Variations in lighting or tool geometry affect image features, complicating comprehensive wear detection and making it challenging to capture suitable images for advanced AI applications [17], [21]. Optimizing hyperparameters is crucial for enhancing the learning process of CNN-based applications [22], [23], [24].

In this study, we present a novel and reliable method for tool wear inspection. The proposed method utilizes a new illumination unit, which enhances the image quality of the endmill cutters. The proposed approach involves capturing high-quality images to identify worn-out regions by employing and fine-tuning CNNs models inspired by CNN architecture [26]. We followed a systematic approach to optimize the hyperparameters and gain new insights into the learning behavior of our proposed CNN architecture. As a result of the pixel-wise evaluation of wear on the cutting edges, tool performance can be thoroughly investigated. Notably, tools with a substantial amount of abnormal wear can be effectively analyzed to initiate improvement measures. These results pave the way for an overall and effective inspection of end mills.

The article is structured as follows: Section II discusses the methodology and derivation of the new approach for tool wear analysis. This section discusses the background and challenges faced by tool manufacturers in image-based inspection of cutting tools. The focus is on their optical properties, particularly their technical and geometric parameters. The CNN-based methods for the detection of normal and abnormal wear are presented in Section III. The learning behavior and performance of various CNN models obtained by changing the hyper-parameters will be discussed. Finally, we verify the segmentation results of the new approach to studying wear behavior. The last section concludes the article.

II. MATERIALS AND METHODS

A. STRUCTURE PARAMETERS AND OPTICAL CHALLENGES

In this section, we address the specific optical challenges associated with integral helical endmills by considering their critical technical and geometrical parameters. Subsequently we introduce the innovative image acquisition system.

Integral spiral endmills are extensively used for milling complex workpieces of arbitrary shapes and materials. The tool's geometry plays a crucial role in the milling process, where different geometric parameters of the cutting edges significantly influence the quality of the machining outcome. Fig. 1 illustrates some essential geometric parameters that need careful consideration during the selection of a milling tool: (i) the cutting tip's design is fundamental in achieving clean and precise cuts, (ii) the center groove enhances stability and facilitates effective chip evacuation, (iii) the first rake angle and peripheral angle are crucial for optimizing the cutting performance of the endmill's, minimizing cutting forces, and ensuring an excellent surface finish, (iv) the helix angle is also of utmost importance for efficient chip removal, reducing heat generation, and promoting seamless cutting, and (v) the relief angle plays a pivotal role in preventing undesirable rubbing or chatter during machining operations. Our novel research methodologies facilitate the utilization of images to enable intelligent customization and adjustments of tool design.

In general, the success of a visual inspection system relies not only on image processing algorithms but also on other critical factors such as optimal optical illumination and reliable hardware for the image acquisition system [27], [28]. The primary task of the optical illumination unit is to ensure that high-quality, stable and reproducible images are captured. The image should enhance the visibility of

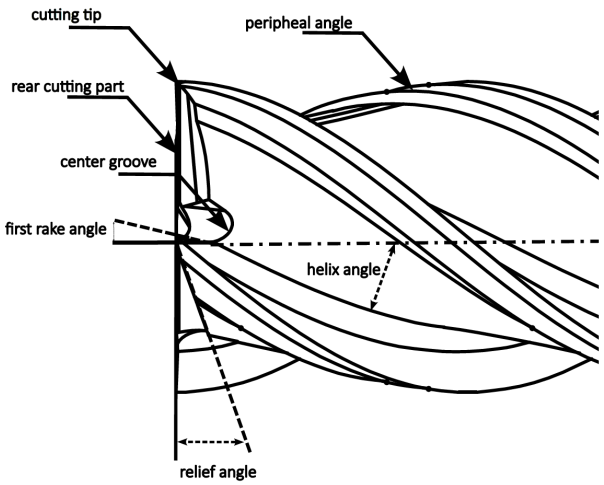

FIGURE 1. Geometric endmill parameters of utmost significance, including the cutting tip, center groove on the rear cutting part, first rake angle, peripheral angle, helix angle, and relief angle.

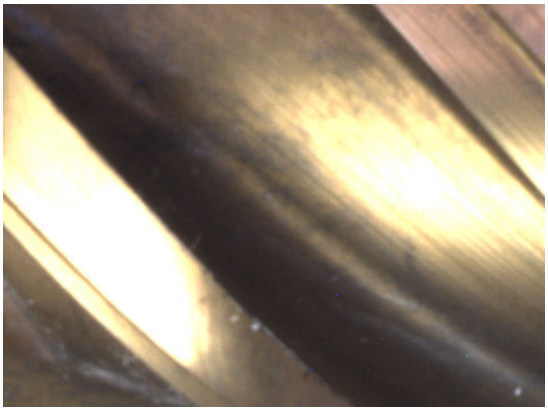

FIGURE 2. Light reflection on TiN coated endmill. The light is reflected back most strongly at the edges of the cutter, whereas shadowing occurs in the inner rake space.

important wear features and minimize undesirable reflections and shadows.

Capturing high-quality images of metallic and spatially curved surfaces using conventional measurement methods is accompanied by many challenges due to multiple light scattering and reflections occurring at various locations on the end mill surface [29], [30]. To enhance the performance of cutting tools, various coatings with high reflection coefficients, such as multi-layered coatings, nanocomposites, and superlattices, are applied. However, these coatings make capturing high-quality images for inspection tasks more challenging, or even impossible and require special illumination techniques.

In machine vision applications for wear detection on milling tools, circular ring arrays of light-emitting diodes (LEDs) [18], direct diffuse illumination [31], and dome lighting [16] are the most used lighting sources. These options offer high illumination intensity and ease of installation on any device, reducing the shadow phenomenon to a certain extent and highlighting relevant features for detection. Although diffuse illumination is mainly used for image-based optical damage detection of reflective surfaces, it does not completely eliminate unwanted reflections.

Undesirable light artifacts generally result from different curvatures and orientations of the tool surface, leading to regular and specular reflections. As shown in Fig. 2, milling exhibits inaccurate color representation in terms of color uniformity and accuracy due to reflections. Even with a direct diffuse light source, avoiding reflection to an acceptable degree remains challenging.

The Phong reflection model describes the composition of the perceived brightness of the detected light intensity (I) of an object. Three components should be considered: ambient, diffuse, and specular light [32]. The captured intensity I is given as:

$$I = I_a K_a + I_l K_a \cos\theta + I_l K_d \cos\theta + I_l K_s \cos\alpha \quad (1)$$

where K_a, K_d, and K_s are the coefficients of ambient light, diffuse light, and specular light, respectively. I_a and I_l are the intensities of the ambient light and direct light from the source, respectively. θ is the angle between the incident light and the normal line of the object's surface. α is the angle between the reflected light and the line of sight, and n is the mirror reflection coefficient.

The ambient component arises from the reflection of nondirectional light from an infinitely large source. The diffuse component accounts for the light scattering on rough surfaces and is and is randomly reflected in all directions. The specular component is based on a perfect mirror reflection, which typically occurs on metal surfaces. Since we focus on characterizing metallic surfaces of an endmill with high optical quality and less surface roughness, the diffuse component can be neglected, and only the reflective and ambient light components should be considered. According to [33], the perceived brightness is then given by:

$$I = K_b I_b + K_d I_d \cos\theta + K_r I_r \quad (2)$$

where K_b is the scale factor of the ambient diffuse light source, I_b is the exposure component of the environmental diffuse reflection, K_d is the scale factor of the direct light source, I_d is the irradiation component, θ is the angle between the incident light and the normal vector of the surface of the object, I_r is the intensity of the reflected light, and K_r is the scale factor of the specular reflection.

In this section, we discuss the innovative approach employed to overcome the challenges of imaging endmills, which are known for their high reflection coefficients. The core of our methodology lies in the adaptation and application of the Phong reflection model to the field of optical imaging. The Phong model, a breakthrough concept in computer graphics, provides an ideal basis for understanding and manipulating light behavior in real-world imaging scenarios. Its effectiveness in modeling specular highlights and local illumination of points on a surface makes it particularly relevant for our purposes [34].

Recognizing the inherent complexities in accurately capturing images of highly reflective surfaces, such as those of endmills [35], our aim was to design an illumination source that could reduce or even avoid specular reflections and enhance the visibility of critical surface features. This customization enables us to selectively minimize the overwhelming specular highlights that often occur in end mill imaging, producing images with balanced homogeneous illumination and improved clarity of surface detail.

In this context, the theoretical basis of our adapted Phong-based illumination technique, the practical implementation and the resulting improvements in image quality during milling are described. This application demonstrates the versatility of the Phong model beyond its conventional digital limitations and sets a new benchmark for the optical imaging of highly reflective industrial tools. Thus, this research paper represents an advanced CNN based tool wear inspection method and imaging technology, while addressing the unique challenges posed by the complex shapes and reflective properties of milling tools.

A schematic diagram of the light reflection behavior at a flat spot of a cutting edge on a milling tool is shown in Fig. 3. According to the Phong model, when light hits the surface of the endmill, it is not only directed in the direction of reflection, but also scattered in other directions with decreasing intensity. Therefore, rendering algorithms can be used to utilize effective images of complex cutting tools with conventional lighting techniques. However, several challenges must be overcome. The complex shape of a milling tool possesses regions with varying surface normals, such as curved surfaces, sharp edges, or intricate details. Obtaining and representing the correct surface normals for these complex shapes can be challenging, especially when dealing with sharp transitions or highly irregular surfaces. Complex milling tools may have regions with different levels of reflectivity, depending on the tool material or surface finish. Accurately capturing and representing these varying specular properties can be challenging, especially when dealing with non-uniform tool surfaces. Furthermore, the curved shape introduces intricate shadowing effects, including self-shadowing, where parts of the tool cast shadows on other parts. The accurate simulation and rendering of these shadowing effects within the Phong model can be computationally intensive. The light can interact with different parts of the tool, depending on the angle, surface orientation, and proximity to other objects. Capturing these complex interactions and correctly applying the Phong model to account for the tool shape can be challenging.

Our newly designed inspection system is shown in Fig. 4. This setup consists of a cylindrical-shaped cavity (1) with a hemisphere on top (2), where light collection and multiple scattering are enhanced. Thirteen LED emitters are placed at equidistant intervals along the U-shaped edge of the hemisphere (3) to enhance multiple light scattering. An enlarged view of the U-shaped inner reflector is shown in Fig. 4(b). The inner walls of the cylinder and hemisphere

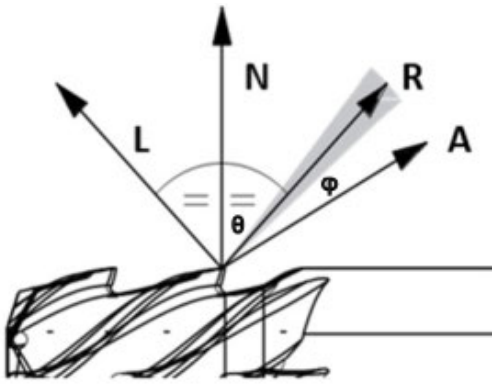

FIGURE 3. The Phong model is used to simulate the reflection behavior of light. The specular component 'R' results in a specular highlight, which depends on the orientation of the surface of the tool relative to the observer (A), the normal vector (N), the point light source (L), and R representing the unit vector directed towards the ideal specular reflection. θ is the viewing angle relative to the specular reflection direction R, and finally, ϕ represents the angle made by L and R with N. As a result, complex milling tools can exhibit areas with varying gloss, shadowing, or reflectivity, influenced by factors such as the tool material, shape, or surface finish.

cavity are coated with white, uniform, and diffuse barium sulfate ($BaSO_4$), which exhibits high reflectivity in the spectral range from 250 nm to 2500 nm. The tool to be inspected is placed in the middle of the enclosure (4). By utilizing the principle of multiple diffuse reflections in the integrating sphere (IS), resulting from its diffuse coating, the ICH spatially integrates the radiation flux from an internal light source. The light emitted from the LEDs at the hemisphere is reflected downwards several times by the $BaSO_4$-coated inner wall of the cavity so that the sample spatial features are uniformly detected by the optical system. Finally, along the exit slit, the electromagnetic beams leave the illumination unit towards the imaging system, creating a homogeneously illuminated image of the tool (4) with reduced unwanted specular and regular reflections according to Eqs. (1) and (2).

The image is then transmitted via the camera's serial interface (6, 7) for further image processing. We have named this new light source the "Integrating Cylindrical Hemisphere" (ICH).

As shown in Fig. 5a and 5b, With the new illumination unit, the image quality can be improved in terms of the following aspects:

1) The uniform and diffuse illumination inside the tool cavity helps to avoid shadowing and reflections on different regions of the tool.
2) Similar to an integrating sphere, the multiple diffuse reflections of the light inside aid in capturing the tool with high color representation (color uniformity and accuracy). This arrangement eliminates shadowing effects and maintains uniform brightness inside the cavity.
3) The uniform lighting enables capturing images with high contrast.

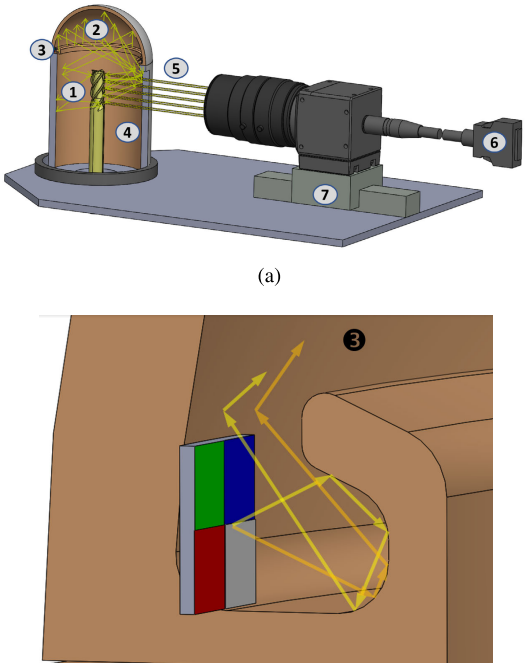

(a)

(b)

FIGURE 4. (a): The enclosure consists of a cylindrical-shaped cavity (1) with a hemisphere (2) on the top. Thirteen LEDs are placed as emitters at equidistant intervals along the U-shaped edge of the hemisphere (3). The tool is placed in the middle of the enclosure (4). The exit port leads to the camera (5). A serial interface connects the camera to the computer (6). The camera is fixed or mounted on a camera mounting plate.(b): An illustration of the U-shaped inner reflector, which enhances multiple light scattering.

4) The uniform lighting conditions allow for capturing reproducible high-quality images.
5) The bright diffuse background facilitates easier separation of the tool from the background, with a clean transition between the tool edges and the background.''

B. CONVOLUTIONAL NEURAL NETWORK

Although CNNs have been around for a while, their earlier use was primarily focused on large-scale classification tasks, such as ImageNet [36] and VOC [37]. In recent years, deep convolutional neural networks (DCNNs) have revolutionized various visual inspection applications [38], [39]. DCNNs have been effectively used for image analysis in optical quality control [40] and in defect detection [41], [42], with a particular focus on metallic surfaces and steel, respectively.

In the context of semantic segmentation U-Net has shown better performance compared to convolutional networks using the sliding window approach. The sliding window approach involves applying a fixed-size window to different parts of the input image to extract features. U-Net's ability to capture context and localize precisely through its ''U-shaped'' architecture leads to improved performance compared to the sliding window approach. A standard U-Net architecture [26] consists of encoder and decoder blocks. The encoder blocks downsample the input image to capture features at different scales using convolutional

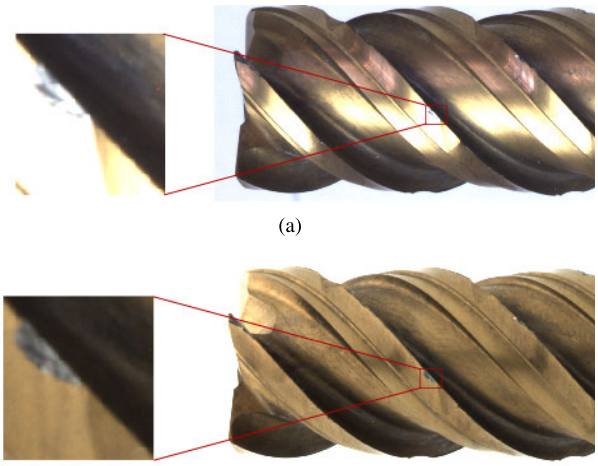

(a)

(b)

FIGURE 5. Comparison of illumination techniques: (a) Direct diffuse illumination and; (b) New light source ICH.

layers, whereas the decoder blocks are responsible for upsampling the feature maps. Transposed convolutions are used for upsampling to recover spatial information lost during downsampling. In this paper, inspired by the U-Net framework we developed a modified version of U-Net for the three-channel wear detection as shown in Fig. 6. This modification allows for precise segmentation.

The proposed network is designed for wear segmentation of the entire end mill. It follows a common neural network architecture, featuring encoder and decoder blocks. The encoder blocks employ convolutional and max-pooling operations, whereas the decoder blocks use upsampling operations to double the image dimensions and replace max-pooling. This process increases the resolution of the output for better feature learning and differentiation between wear and abnormal wear. Fig. 6 illustrates the model's structure, with the contracting path using multiple convolutional and max-pooling layers for hierarchical feature capture and input compression.

The customized CNN architecture consists of four encoding and decoding blocks utilized for images with three channels (RGB) to maintain visual information. The expanding path employs upsampling and concatenation operations to recover spatial information and generate pixel-wise predictions. DO operations are applied after each block, and skip connections connect the encoder blocks to decoder blocks via long arrows. The contracting path in the model consists of repeated 3×3 convolution operations controlled by ReLU activation and 2×2 max pooling with stride 2 for downsampling, doubling the feature channels. The expansive path performs upsampling followed by 2×2 ''up-convolution'' to reduce feature channels by half. To address the loss of border pixels, concatenation is performed with the corresponding cropping feature map from the contracting path. Two 3×3 convolutions with ReLU activations are then applied, followed by a 1×1 convolution at the final

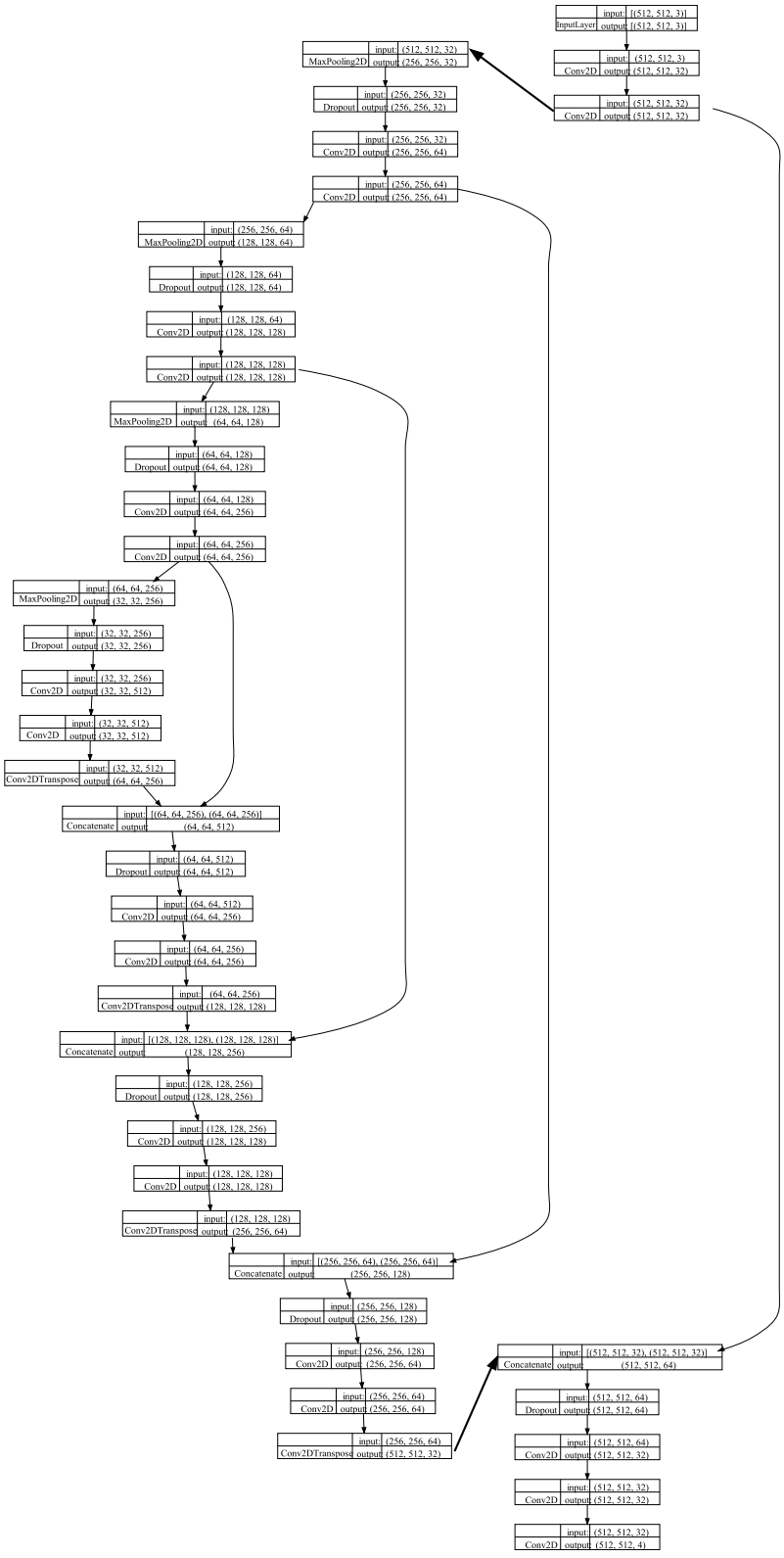

FIGURE 6. CNN Architecture for normal and abnormal wear segmentation.

level to match the feature vectors to the desired number of four classes: Abnormal Wear, Normal Wear, Tool, and Background. The bottleneck layer between the encoding and decoding blocks represents the latent space that holds the most compressed representation of the training dataset. To achieve seamless tiling of the output segmentation map,

the input tile size is chosen so that all 2 × 2 max-pooling operations are applied to layers with the same x and y size. As there are multiple classes, the pixel-weighted soft-max sparse cross-entropy loss is used to account for unbalanced classes in semantic segmentation. The pixel-weighted Softmax Sparse Cross-Entropy Loss is defined as:

$$l(I) := -\sum_{x\in\Omega} w(x) log \frac{exp(\hat{y}_{y(x)}(x))}{\sum_{k=0}^{K} exp(\hat{y}_k(x))} \tag{3}$$

where x is a pixel in the image domain Ω, $\hat{y}_k : \Omega \rightarrow \mathbb{R}$ is the predicted score for class $k \in \{0, \ldots, K\}$, K is the number of classes, and $y :\rightarrow \{0, \ldots, K\}$ is the ground truth segmentation map. Thus, $\hat{y}_{y(x)}(x)$ is the predicted score for the ground truth class $y(x)$ at the position x. As defined above, $w : \Omega \rightarrow \mathbb{R}_{\geq 0}$ is the pixelwise-loss-weight map. Loss weighting has been used to achieve class balancing and address areas with no annotations, utilizing the weight map w_{bal}. Additionally, instance separation is enforced through the use of weight w_{sep}, as explained in the subsequent sections. The ultimate loss weights are determined as follows:

$$w := w_{bal} + \lambda w_{sep} \tag{4}$$

where $\lambda \in R_{\geq 0}$ controls the importance of instance separation.

$$w_{\text{bal}}(x) := \begin{cases} 1 & \text{if } y(x) > 0, \\ v_{\text{bal}} & \text{if } y(x) = 0, \\ 0 & \text{if } y(x) \text{ is unknown.} \end{cases} \tag{5}$$

We observed slightly better segmentation results when replacing the step-shaped cutoff at the edges of the foreground objects with a smoothly decreasing Gaussian function for the weighted loss computation; therefore, we define

$$w'_{\text{bal}}(x) := \begin{cases} 1 & \text{if } y(x) > 0, \\ v_{\text{bal}} + (1 - v_{\text{bal}}) \cdot \exp\left(-\frac{d_1^2(x)}{2\sigma_{\text{bal}}^2}\right) & \text{if } y(x) = 0, \\ 0 & \text{if } y(x) \text{ is unknown.} \end{cases} \tag{6}$$

where $d_1(x)$ is the distance to the closest foreground object, and σ_{bal} is the standard deviation of the Gaussian. We approximate the ridge width at each pixel by the sum of the distance d_1 to its nearest instance and the distance d_2 to its second nearest instance. From this, we compute the weight map as

$$w_{\text{sep}}(x) := \exp\left(-\frac{(d_1(x) + d_2(x))^2}{2\sigma_{\text{sep}}^2}\right) \tag{7}$$

which decreases following a Gaussian curve with standard deviation σ_{sep}.

C. THE OVERALL PROCESS FOR INTEGRAL SPIRAL ENDMILL TOOL WEAR DETECTION

The methodology for the wear analysis is delineated in the wear inspection process flowchart (see Fig. 7). Initially, a sequence of tool images is acquired through an imaging system optimized for low reflectance and high resolution (a). Subsequent image processing delineates the region of interest and standardizes the image dimensions (b). A targeted mask is generated to emphasize the prospective wear locations (c). This mask, along with corresponding image data, is segmented into datasets conducive for neural network analysis (d). The previously processed image input is then introduced to a pre-trained neural network model, specifically a CNN designed for wear feature identification (e). The model scrutinizes the input to identify wear patterns based on its trained feature set (f). Consequently, the model outputs a segmented mask that categorizes the wear regions as normal or abnormal within the image (f). These individual predictions are amalgamated into an integrated image representation of the tool (g). The resultant data is then utilized for further evaluation or subsequent procedures.

D. DATASET

Due to the huge labeling effort required for the training datasets, we decided to focus our use cases on two distinct types of tools with different coatings: TiCN and TiN.

TiCN is a widely-used coating for endmills, known for its durability and application in machining steel and cast iron. TiN is a popular coating for various cutting tools, renowned for its wear resistance and low friction properties, allowing it to be used on diverse materials, including steel and cast-iron inserts.

Fig. 8 illustrates the typical dataset comprising images of endmills captured using our new illumination technique for training the U-Net models. To increase the variability the dataset consists of eight different tools, four with TiCN coating and four with TiN coating.

Each individual tool was captured from eight different angles, at 45-degree intervals, resulting in a total of eight high-resolution images. The images were then cropped into 24 sub-images with dimensions of 512 × 512 pixels (Fig. 9), to preserve visual information that might otherwise be lost through data compression. Additionally, assigning each subimage to a matrix helps us to analyze wear patterns in specific regions of an image and to ensure a structured representation. Thus, a total of 768 images were generated for training and testing the neural network for each tool. The participating employees came from Linner Werkzeug Schleif Fabrik (https://herionlinner.com/linner-gmbh-werkzeugfabrik/(accessed on 30 May 2024)), a company specializing in tool regrinding. Furthermore, fragmenting the image allows parallel wear detection on graphics processing units (GPUs) and accelerates the seamless combination of predictions from individual fragments into a complete image.

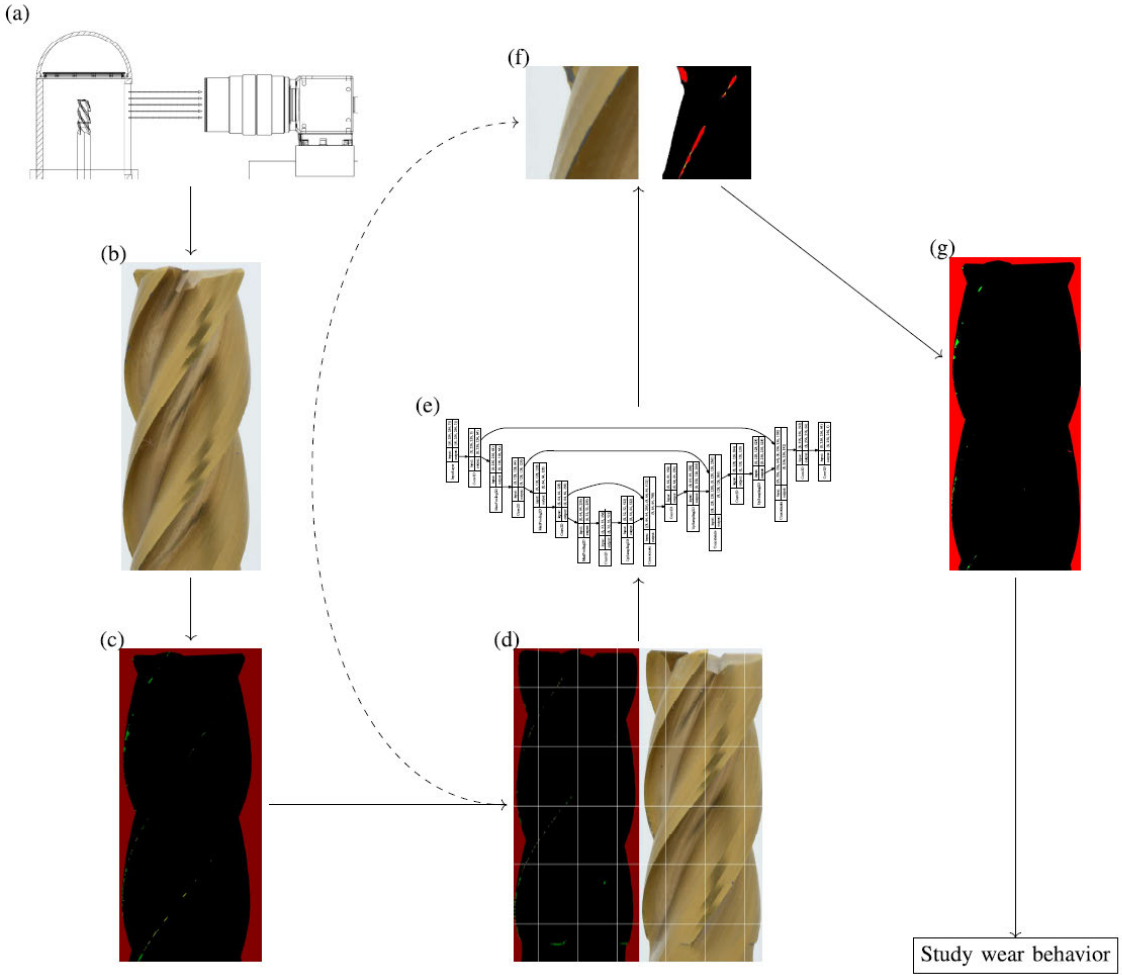

FIGURE 7. Flowchart of the Wear Inspection Process. (a) New camera system. (b) Captured image. (c) Mask of normal wear and abnormal wear. (d) Data set fragmentation. (e) Trained CNN model. (f) Normal and abnormal Wear prediction. (g) Merged tool image for analysis.

During the labeling process, there were various challenges, particularly regarding the darker TiCN coated milling tool, which shows more subtle wear with darker wear characteristics that cannot be properly recognized and assigned to the corresponding class. We marked instances with a polygon. The number of instances varied depending on the tool type and the amount and types of wear. The TiCN tool shows significantly more normal and abnormal wear pixels compared to the TiN tool. This variety in the data set highlights the challenges for proper annotation and can affect the training performance. The amount of instances of the four different classes used to train the models are summarized in table 1.

TABLE 1. Instance distribution in datasets.

Tool Coating	Class background	Class normal wear	Class abnormal wear	Class Tool
TiCN	432	404	806	768
TiN	432	770	532	768

E. TRAINING STRATEGY

We implemented our models on the TensorFlow platform and trained them on NVIDIA GeForce RTX 4090 GPUs, which have 24GB of memory. The following hyperparameters: learning rate (LR), dropout (DO), and batch sizes (BS) can influence the model's performance.

The learning rate (LR) determines the step size at each iteration while moving toward a minimum of the loss function. Dropout (DO) is a regularization technique used to improve model performance and avoid overfitting. During training, neurons are randomly ignored or "dropped out," allowing the network to learn more robust features and generalize better. The batch size (BS) defines the number of training examples used in one iteration during the training process.

In our study, the LR was set to 0.001 and 0.0001, respectively. We experimented with different dropout rates for each layer: 0.3, 0.5, and 0.8, and different batch sizes: 8 and 16. For each parameter combination, we trained the model using sparse categorical cross-entropy, and the network was trained for 70 epochs.

F. TRAINING PERFORMANCE WITH VARIED HYPER-PARAMETERS

Fig. 11 and Fig. 12 show the normalized training and validation loss curves of the different models trained with

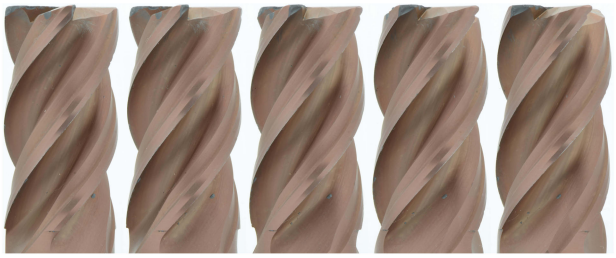

(a) Dataset: TiCN-coated tool

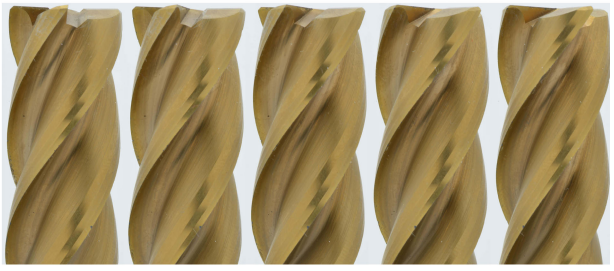

(b) Dataset: TiN-coated tool

FIGURE 8. Series of images captured by the acquisition system ICH. TiCN coated tool (a) and TiN coated tool (b).

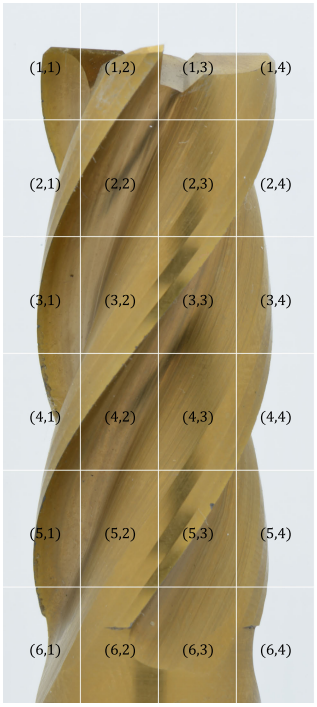

FIGURE 9. Fragmentation of an image of an integral spiral endmill into 24 parts.

different hyperparameters for the two data sets of the tool with TiN coating and the tool with TiCN coating.

Considering the loss curves for the model trained on TiN-coated tools (Fig. 11a) with a DO rate of 0.5, a BS of 8 and an LR of 0.001, an increased variation of the training and validation loss can be seen in the first epochs

(a) Labeled dataset: TiNC coated tool

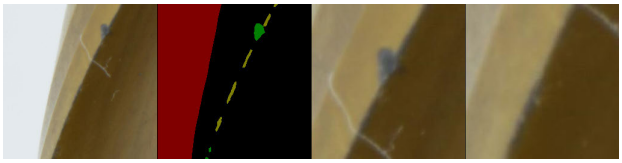

(b) Labeled dataset: TiN coated tool

FIGURE 10. Dataset annotation example for the semantic segmentation of wear on two types of coated tools: TiCN coated tool (a) and TiN coated tool (b). The wear is divided into two distinct classes - "yellow" for normal wear and "green" for abnormal wear. The additional two other classes are: "red" for the background and "black" for the tool itself. On the right side, a magnified view displays the wear classes for better visibility.

and increasingly from the middle to the end of the epochs, indicating an unstable training performance especially in the late epoch phase. The training behavior of models without drop-out tends to show a faster learning performance. However, despite a sharp decline, however, the learning curves of validation and training losses show a certain disproportionality with peaks that indicate poor to unstable learning behavior. Similar training behavior, but slightly less noticeable, is the training behavior of the model when using a of DO 0.3. Despite the good convergence behavior in the first epochs, some peaks in the validation losses occur in the first epoch phases, but also increasingly in later epochs, which makes it clear that training and generalization are improved but can also become unstable in the final phase.

As can be seen in Fig. 11b, a lower LR 0.0001 shows a more stable training and validation process across all DO rates, indicating improved training performance and generalization, with no tendencies towards under- or over-fitting. At a higher BS (16) and higher LR, Fig. 11c shows an improved learning behavior with a slightly more balanced ratio between the training and validation losses. However, the validation losses show increasing oscillating peaks, especially for models with DO of 0.3 and 0.5, indicating poor generalization.

Finally, Fig 11d with a smaller LR 0.0001 and stack size of 16 shows the best convergence behavior for both the training and validation curves of the models across all DO rates. In particular, the model with a DO of 0.3 appears to exhibit particularly stable learning behaviour and generalization.

As shown in Fig. 12a and 12b, the TiCN-coated tools show similar trends to the TiN-coated tools. As can be seen in Fig. 12c, higher bs (16) and a DO rate of 0.5 and 0.3 for TiCN-coated tools lead to an even stronger unstable generalization compared to TiN-coated tools, indicating a possibly too intensive regularization. Similar to the TiN-coated tools, a lower LR (0.0001) in combination with a larger BS (16) has a positive effect on the learning and convergence behavior at all DO rates, as shown in Fig. 12d. From the results,

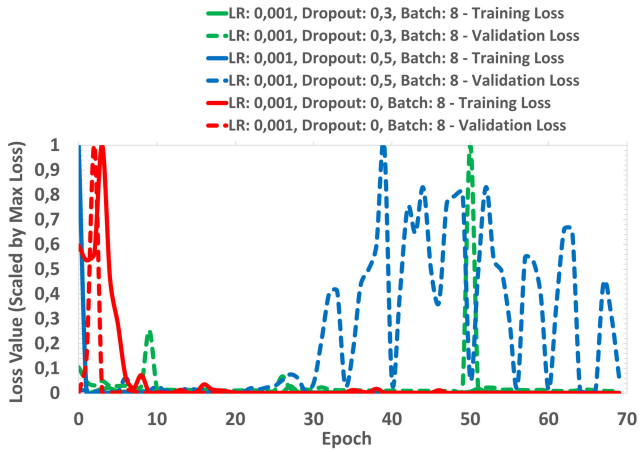

(a) Loss curves for a model with LR of 0.001, exploring DO rates of 0.3 and 0.5, and bs of 8.

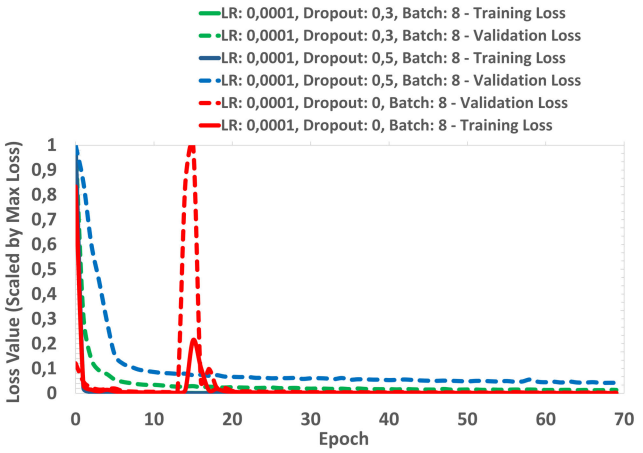

(b) Loss curves for a model with a lower LR of 0.0001, using DO rates of 0.3 and 0.5, and BS of 8.

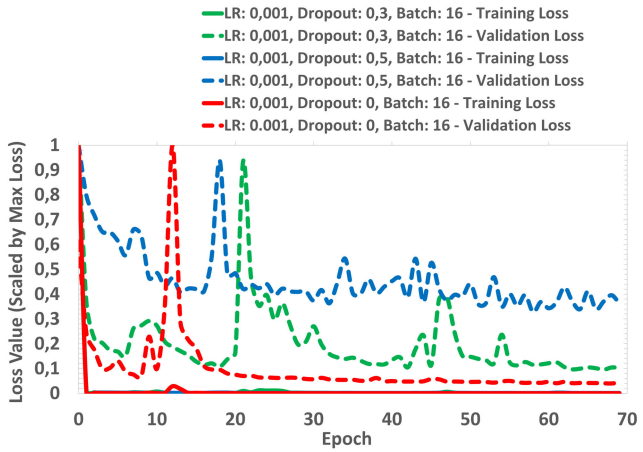

(c) Loss curves with a LR of 0.001, DO rates of 0.3 and 0.5, and a higher BS of 16.

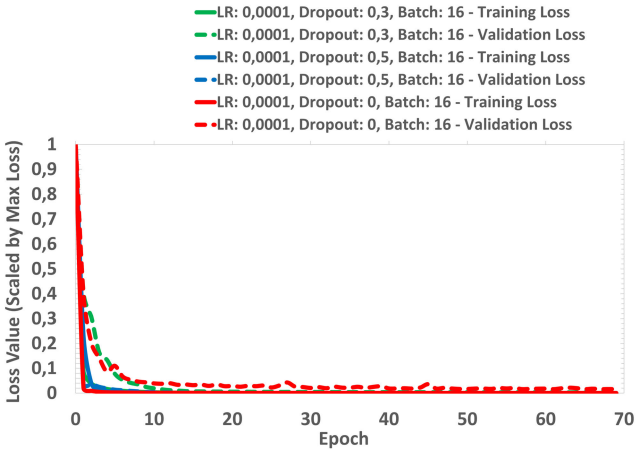

(d) Loss curves for models trained with a LR of 0.0001 and BS of 16, varying DO between 0.3, 0.5, and no DO.

FIGURE 11. Validation and training loss curves of models with different hyper-parameters LR, BS, and DO to illustrate the learning performance on TiN-coated milling tools. Each sub-figure analyzes the impact of these parameters on training dynamics and model stability.

a moderate DO rate of 0.3, a small LR and a large BS (16) for both coating types provides a good balance between adaptability and generalization capability and thus these hyperparameters can be well matched to the specific image information of the tool types due to the reflectance and absorption properties of the coatings used for a robust CNN model.

G. CNN MODELS FOR SEMANTIC SEGMENTATION OF TOOL WEAR

The learning behavior and generalization ability of different models have already been investigated in an ablation study by varying the hyper parameters. Similarly, in this section, we discuss the segmentation results of our ablation study on the detection of wear patterns on TiN and TiCN coated milling tools for the proposed network architecture. The influence of hyperparameters, including LR, BS size, and the application of DO, was investigated to find the model, with the best segmentation performance, in its first application on a test dataset. To evaluate the results, we use the well-known metric Intersection over Union (IoU). The score, also known as the Jaccard similarity coefficient, quantifies the proportion of correctly classified pixels for each class by dividing the number of true positives by the union of the predicted and actual positives:

$$IoU_i = \frac{TP_i}{TP_i + FP_i + FN_i} \tag{8}$$

Here,i stands for the class and 'True Positive' (TP) refers to pixels correctly predicted as belonging to the ground truth class. 'False Positive' (FP) refers to pixels incorrectly predicted as belonging to the ground truth class. 'False Negative' (FN) refers to pixels that are incorrectly predicted as not belonging to the target class To evaluate the models on their overall performance, we introduce a weight adjustment of the underrepresented classes such as normal and abnormal

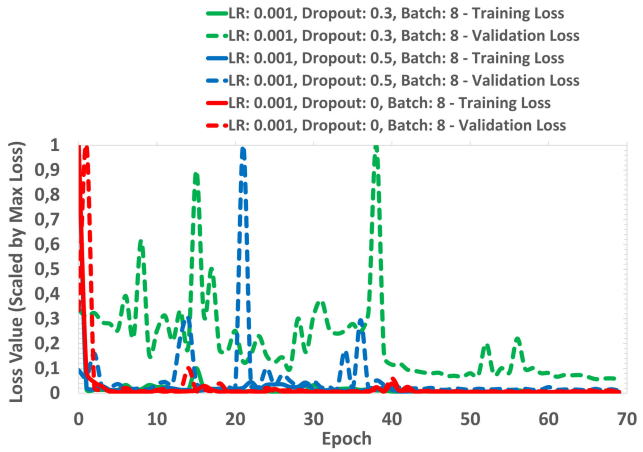

(a) Loss curves for the model with a LR of 0.001, DO variations of 0.3 and 0.5, and BS 8.

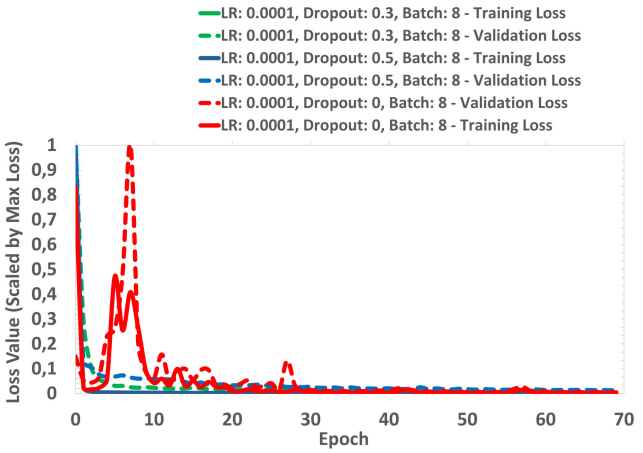

(b) Loss curves for the model with a reduced LR of 0.0001, employing DO settings of 0.3 and 0.5 with BS of 8.

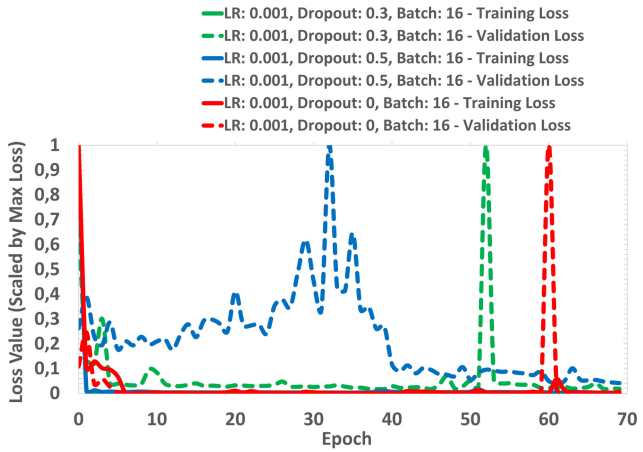

(c) Loss curves for the model using a LR of 0.001 with DO 0.3 and 0.5, and a BS of 16.

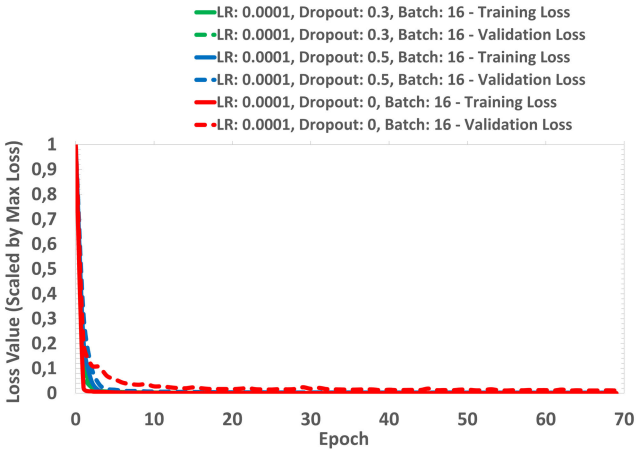

(d) Loss curves for the model with a lower LR of 0.0001 and BS of 16.

FIGURE 12. **Loss curves of models with different hyper-parameters LR, BS, and DO to illustrate the learning performance on TiCN-coated milling tool.**

wear compared to the overrepresented classes such as background and damage-free tool surface. The formula to determine the weights for a weighted average calculation (WMIoU) is described below:

1) Determine the class frequencies by counting the occurrences of each class in the dataset to obtain N_1, N_2, N_3, and N_4.
2) Calculate the inverse frequencies for each class as follows:

$$\frac{1}{N_1}, \frac{1}{N_2}, \frac{1}{N_3}, \text{ and } \frac{1}{N_4}. \tag{9}$$

3) Normalize the weights by summing all the inverse frequencies and then dividing each inverse frequency by this sum to get weights w_1, w_2, w_3, and w_4 that add up to 1:

$$w_i = \frac{\frac{1}{N_i}}{\sum_{j=1}^{4} \frac{1}{N_j}} \tag{10}$$

4) Apply the weights to calculate the weighted mean IoU:

$$\text{WMIoU} = w_1 \cdot IoU_1 + w_2 \cdot IoU_2 + w_3 \cdot IoU_3 + w_4 \cdot IoU_4 \tag{11}$$

By using inverse frequencies, we ensure that underrepresented classes (with a lower frequency N_j) are given more weight in the calculation. This increases the influence of the underrepresented class on the average performance evaluation of the model.

Table 2 and Table 3 show the segmentation results mIoU of the four classes: Background, Tool, Abnormal Wear and Normal Wear for both data sets the TiN and TiCN coated tools. The weighted overall performance metric WMIoU was calculated to provide a measure of the overall segmentation accuracy despite the unbalanced class frequency. The performance of each model was analyzed by varying the different hyperparameters: LR, DO and BS. First, we consider the results from the TiN-coated tool. Almost all models provide

TABLE 2. Comparison of the segmentation results as mIoU for the four classes background (BG), tool(T), abnormal wear(AW), normal wear(NW) and the overall performance WMIoU on the test data set of a TiN-coated milling cutter with variation of the hyperparameters LR, dropuot and BS.

Model	BG [IoU]	T [IoU]	AW[IoU]	NW [IoU]	WMIoU [IoU]	LR	BS	DO
MTiN 0	**1.00**	0.99	0.77	0.62	0.65	0.001	8	0
MTiN 1	**1.00**	0.98	**0.79**	0.69	**0.71**	0.001	8	0.3
MTiN 2	**1.00**	0.99	0.66	**0.71**	0.70	0.001	8	0.5
MTiN 3	**1.00**	**1.00**	0.76	0.60	0.64	0.001	16	0
MTiN 4	**1.00**	0.98	0.64	**0.71**	0.70	0.001	16	0.3
MTiN 5	**1.00**	0.96	0.61	**0.71**	0.69	0.001	16	0.5
MTiN 6	**1.00**	0.99	0.70	0.52	0.56	0.0001	8	0
MTiN 7	**1.00**	0.96	0.71	0.63	0.65	0.0001	8	0.3
MTiN 8	**1.00**	**1.00**	0.65	0.69	0.68	0.0001	8	0.5
MTiN 9	**1.00**	0.97	0.69	0.37	0.44	0.0001	16	0
MTiN 10	**1.00**	0.96	0.78	0.45	0.53	0.0001	16	0.3
MTiN 11	**1.00**	0.96	0.52	0.61	0.59	0.0001	16	0.5

TABLE 3. Comparison of the segmentation results as mIoU for the four classes background (BG), tool(T), abnormal wear (AW), normal wear (NW) and the overall performance WMIoU on the test data set of a TiCN-coated milling cutter with variation of the hyperparameters LR, dropuot and BS.

Model	BG [IoU]	T [IoU]	AW[IoU]	NW [IoU]	WMIoU [IoU]	LR	BS	DO
MTiCN 0	0.99	0.69	0.51	0.09	0.20	0.001	8	0
MTiCN 1	0.99	**0.96**	0.52	0.52	0.60	0.001	8	0.3
MTiCN 2	0.99	0.83	0.34	**0.59**	0.64	0.001	8	0.5
MTiCN 3	**1.00**	0.85	0.43	0.41	0.49	0.001	16	0
MTiCN 4	0.99	0.81	0.54	0.50	0.56	0.001	16	0.3
MTiCN 5	0.99	0.83	0.46	0.59	0.63	0.001	16	0.5
MTiCN 6	0.99	0.79	0.44	0.24	0.34	0.0001	8	0
MTiCN 7	0.99	0.92	**0.61**	**0.60**	**0.65**	0.0001	8	0.3
MTiCN 8	0.99	0.92	0.54	0.48	0.56	0.0001	8	0.5
MTiCN 9	0.99	0.80	0.59	0.46	0.53	0.0001	16	0
MTiCN 10	0.99	0.78	0.50	0.47	0.53	0.0001	16	0.3
MTiCN 11	0.99	0.79	0.42	0.42	0.49	0.0001	16	0.5

impressive segmentation results for the background with a mIoU for all models with a 1.00 models. The segmentation class tool also shows outstanding performance, ranging from 0.96 to 1.00. This means that the models can fully distinguish the classes, tool and wear, from the background from the class tool, normal and abnormal wear.

For studying the wear behavior the segmentation results of normal and abnormal are of particular relevance. For the TiN-coated tool, the model MTiN 1(LR:0.001, BS:8, DO:0.3) provides the best wear identification results with an mIoU of 0.71 for abnormal wear and 0.69 for the normal wear class. Considering the weighted overall performance across all classes, MTiN 1 also performs best with a WMIoU of 0.71. When evaluating the models with the test dataset with respect to the hyper-parameters, the expectation differs from the expected trend of the validation curves in Fig. 8 and 9. Models trained with a higher LR of 0.001 in tend to outperform the test data set. This may be due to the fact that the test data may be more similar to the training data than the validation data.

Consider now the segmentation results of the TiCN coated tool. Similar to the TiN-coated tool, all models deliver good segmentation results for the background. This means that we can also distinguish the tool from the background particularly well here. However, the models perform worse in the tool class. The MTiCN 1 model with hyperparameters (LR:0.001, BS:8, DO:0.3) provides the best segmentation results with regard to the tool class. For the classes of interest, normal and abnormal wear, the MTiCN 7 (LR:0.0001, BS:8, DO:0.3) model provides the best segmentation result of 0.61 for abnormal wear and 0.60 for normal wear, respectively. It appears that normal wear is often more difficult to identify than abnormal Wear due to its more subtle nature, particularly with TiCN tools. Where as TiN-coated tool models with a lower LR of 0.001 tend to give better results, the TiCN-coated

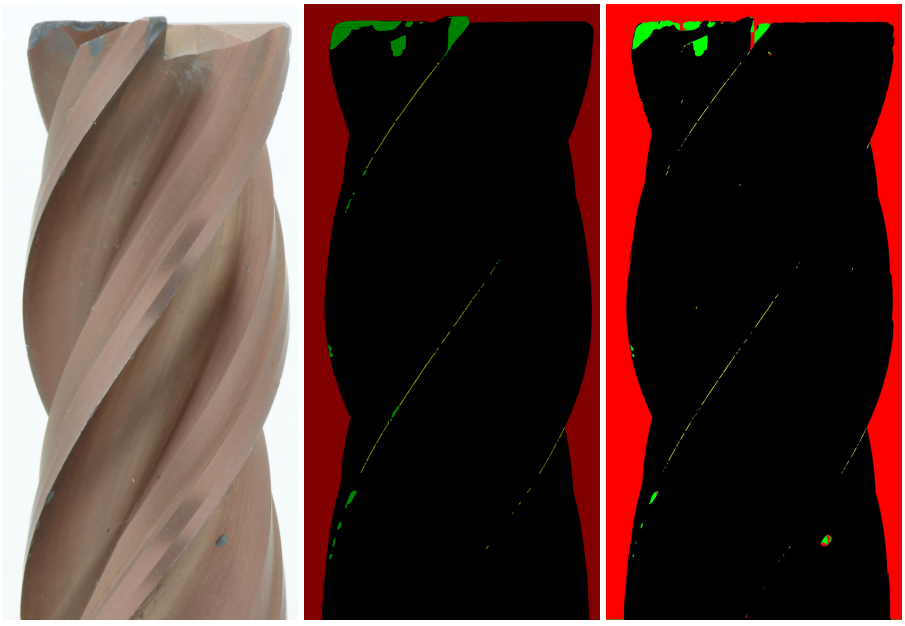

Captured image (a) Ground Truth (b) Prediction (c)

FIGURE 13. Illustration of the segmentation results of a TiCN-coated milling tool: (a) raw images captured by our inspection system; (b) ground of truth mask; (c) segmentation results predict by the MTiCN 7 model.

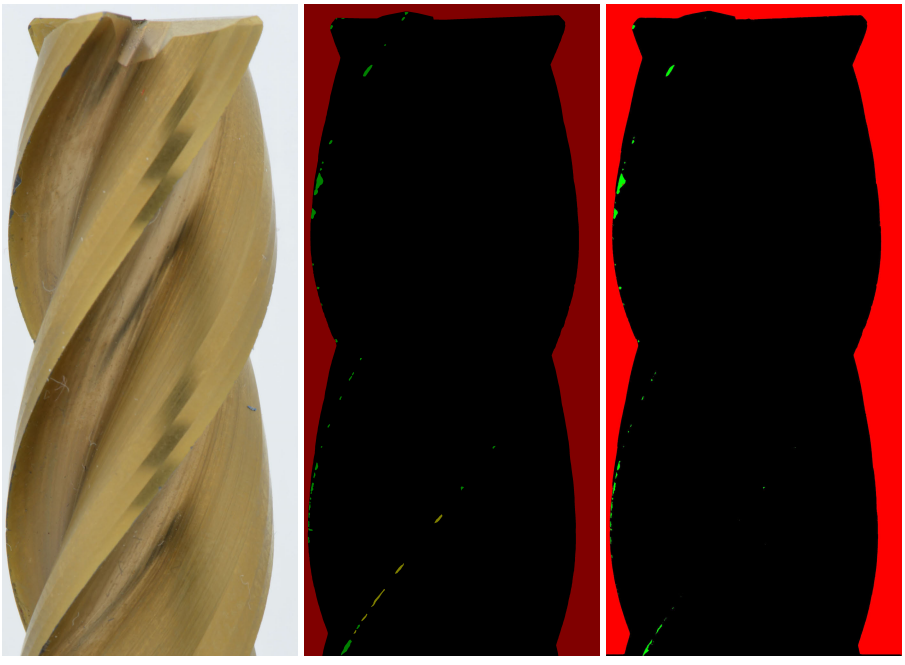

Captured image (a) Ground Truth (b) Prediction (c)

FIGURE 14. Ilustration of the segmentation results of a TiN coated milling tool: (a) the raw images captured by our inspection system; (b) the ground of truth mask; (c) the segmentation results predicted by the MTiN 1 model.

tool models perform slightly better at lower learning rates. In summary, the models of both tools show successful mIoU values, which demonstrates the stability and usability of wear analysis of cutting tools. The MTiN models trained and tested on TiN data set, perform better in the identification of abnormal and normal wear, this is because the TiN coated

tool shows more obvious abnormal wear patterns, which can be more accurately distinguished from normal wear as a feature, wherea the TiCN coated tool shows significantly less abnormal wear, which is also more difficult to distinguish from normal wear due to its subtle nature. The regulation method with a DO of 0.3 seems to have a positive effect on all models, whereas the LR plays a smaller role and the BS seems irrelevant for the training process.

To identify, locate, and analyze the wear behavior the segmentation results of the best-performing models of the proposed model are shown visually in Fig. 13 and Fig. 14. The segmentation results of the TiCN-coated tool (Fig. 13) clearly show that abnormal wear occurs on the cutting tip and rear cutting part. This indicates that a careful analysis of the machining conditions, tool material, and cutting edge geometry can be beneficial in identifying issues and improving tool life, thereby enabling the implementation of targeted countermeasures. Additionally, normal wear through the rake angle is also recognizable.

Similarly, the segmentation results of the TiN-coated milling tool are presented in Fig. 14. Abnormal wear appears to play a less significant role in comparison to the TiCN-coated tool, which can be attributed to the proper utilization of the tool and the appropriate selection of geometric parameters.

III. CONCLUSION

This paper presents a novel method for automating the wear analysis of cutting tools. We employed a custom illumination unit tailored specifically for end mill wear inspection, enabling the generation of high-quality, low-reflection images conducive to our CNN architecture. Utilizing these distinctive images, we compiled datasets featuring two different tools coated with TiN and TiCN for training customized CNN models. To optimize the CNN's performance in detecting normal and abnormal wear, we experimented with various training parameters, analyzing the models' behavior through detailed examination of loss curves and segmentation of four classes (background, tool, normal wear, and abnormal wear). Our findings indicate that a moderate DO rate of 0.3 strikes an optimal balance between adaptability and generalization capability for both coating types. Thus, these hyper parameters can be well adapted to the specific image information of the tool types due to the reflection and absorption properties of the coatings used.

We found that the MTiN 1 model (LR: 0.001, BS: 8, DO: 0.3) provides the best results in wear detection, with an mIoU of 0.79 for abnormal wear and 0.69 for normal wear. Looking at the overall weighted performance across all classes, MTiN 1 performs with a WMIoU of 0.71 best. For the TiCN coated milling tool for the classes normal and abnormal wear, the MTiCN 7 model provides the best segmentation result of 0.61 for abnormal wear and 0.60 for normal wear, concluding a DO of 0.3 mostly improves the model performance for wear detection. The proposed method was primarily tested on tools with TiN and TiCN coatings. However, in real-world scenarios, tools can have other materials or coatings. The tools can be used for different workpieces with various materials and coatings, leading to more distinct wear characteristics that make annotations across different tool types more time consuming, inconsistent and difficult for real-world applications. In the future, we will use the system for other cylindrical cutting tools or other construction parts for inspection tasks, which may require an extended data set and customized optimization of the acquisition system in its current form.

ACKNOWLEDGMENT

The authors specially thank the consortium partners for their indispensable collaboration in this research project. Linner GmbH Tool Factory provided invaluable industry insights with Ludwig Linner the primary sponsor and together with Mühenad Bilal responsible contact for the project. Technical guidance and academic supervision were generously offered by Prof. Markus Bregulla from the AIMotion Bavaria Department, Technical University of Ingolstadt (THI). They acknowledge the commitment and support of all team members and contributors who have facilitated the merging of high-quality research with practical application.

COMPETING INTERESTS

The illumination technique used in their research for the wear inspection system is based on the European Patent EP1430720, developed by Mühenad Bilal and Christian Mayer. This specific illumination approach has been modified for wear characterization and enables the identification of tiny wear features that cannot be detected with conventional inspection systems.

REFERENCES

[1] M. Malekian, S. S. Park, and M. B. G. Jun, "Tool wear monitoring of micro-milling operations," *J. Mater. Process. Technol.*, vol. 209, no. 10, pp. 4903–4914, Jun. 2009.

[2] J. Karandikar, T. McLeay, S. Turner, and T. Schmitz, "Tool wear monitoring using Naïve Bayes classifiers," *Int. J. Adv. Manuf. Technol.*, vol. 77, nos. 9–12, pp. 1613–1626, Apr. 2015.

[3] Y. Zhou and W. Xue, "Review of tool condition monitoring methods in milling processes," *Int. J. Adv. Manuf. Technol.*, vol. 96, nos. 5–8, pp. 2509–2523, May 2018.

[4] M. S. H. Bhuiyan, I. A. Choudhury, M. Dahari, Y. Nukman, and S. Z. Dawal, "Application of acoustic emission sensor to investigate the frequency of tool wear and plastic deformation in tool condition monitoring," *Measurement*, vol. 92, pp. 208–217, Oct. 2016.

[5] W.-H. Sun and S.-S. Yeh, "Using the machine vision method to develop an on-machine insert condition monitoring system for computer numerical control turning machine tools," *Materials*, vol. 11, no. 10, p. 1977, Oct. 2018.

[6] X. Li, "A brief review: Acoustic emission method for tool wear monitoring during turning," *Int. J. Mach. Tools Manuf.*, vol. 42, no. 2, pp. 157–165, Jan. 2002.

[7] H. V. Ravindra, Y. G. Srinivasa, and R. Krishnamurthy, "Acoustic emission for tool condition monitoring in metal cutting," *Wear*, vol. 212, no. 1, pp. 78–84, Nov. 1997.

[8] D. O'Sullivan and M. Cotterell, "Temperature measurement in single point turning," *J. Mater. Process. Technol.*, vol. 118, nos. 1–3, pp. 301–308, Dec. 2001.

[9] E. P. Carden and P. Fanning, "Vibration based condition monitoring: A review," *Struct. Health Monitor.*, vol. 3, no. 4, pp. 355–377, Dec. 2004.

[10] C. Drouillet, J. Karandikar, C. Nath, A.-C. Journeaux, M. El Mansori, and T. Kurfess, "Tool life predictions in milling using spindle power with the neural network technique," *J. Manuf. Processes*, vol. 22, pp. 161–168, Apr. 2016.
[11] D. E. Dimla Sr. and P. M. Lister, "On-line metal cutting tool condition monitoring: I: Force and vibration analyses," *Int. J. Mach. Tools Manuf.*, vol. 40, no. 5, pp. 739–768, 2000.
[12] A. Fernández-Valdivielso, L. L. De Lacalle, G. Urbikain, and A. Rodriguez, "Detecting the key geometrical features and grades of carbide inserts for the turning of nickel-based alloys concerning surface integrity," *Proc. Inst. Mech. Eng. C, J. Mech. Eng. Sci.*, vol. 230, no. 20, pp. 3725–3742, Dec. 2016.
[13] P. Ong, W. K. Lee, and R. J. H. Lau, "Tool condition monitoring in CNC end milling using wavelet neural network based on machine vision," *Int. J. Adv. Manuf. Technol.*, vol. 104, nos. 1–4, pp. 1369–1379, Sep. 2019.
[14] W. Wang, Y. S. Wong, and G. S. Hong, "Flank wear measurement by successive image analysis," *Comput. Ind.*, vol. 56, nos. 8–9, pp. 816–830, Dec. 2005.
[15] W. H. Wang, G. S. Hong, and Y. S. Wong, "Flank wear measurement by a threshold independent method with sub-pixel accuracy," *Int. J. Mach. Tools Manuf.*, vol. 46, no. 2, pp. 199–207, Feb. 2006.
[16] W. Wei, J. Yin, J. Zhang, H. Zhang, and Z. Lu, "Wear and breakage detection of integral spiral end milling cutters based on machine vision," *Materials*, vol. 14, no. 19, p. 5690, Sep. 2021.
[17] T. A. Rashid, J. Majidpour, R. Thinakaran, M. Batumalay, D. A. Dewi, B. A. Hassan, H. Dadgar, and H. Arabi, "NSGA-II-DL: Metaheuristic optimal feature selection with deep learning framework for HER2 classification in breast cancer," *IEEE Access*, vol. 12, pp. 38885–38898, 2024.
[18] X. Wu, Y. Liu, X. Zhou, and A. Mou, "Automatic identification of tool wear based on convolutional neural network in face milling process," *Sensors*, vol. 19, no. 18, p. 3817, Sep. 2019, doi: 10.3390/s19183817.
[19] Z. Li, J. Tang, Y. Li, and J. Bai, "Investigation on surface integrity in novel micro-EDM with two-dimensional ultrasonic circular vibration (UCV) electrode," *J. Manuf. Processes*, vol. 76, pp. 828–840, Apr. 2022, doi: 10.1016/j.jmapro.2022.03.004.
[20] C. Gkournelos, N. Kousi, A. C. Bavelos, S. Aivaliotis, C. Giannoulis, G. Michalos, and S. Makris, "Model based reconfiguration of flexible production systems," *Proc. CIRP*, vol. 86, pp. 80–85, Jan. 2019, doi: 10.1016/j.procir.2020.01.042.
[21] Y. Li, S. Tian, C. Wu, and M. Tanaka, "Experimental sensing of molten flow velocity, weld pool and keyhole geometries in ultrasonic-assisted plasma arc welding," *J. Manuf. Processes*, vol. 64, pp. 1412–1419, Apr. 2021, doi: 10.1016/j.jmapro.2021.03.005.
[22] H. K. Hamarashid, B. A. Hassan, and T. A. Rashid, "Modified-improved fitness dependent optimizer for complex and engineering problems," *Knowl.-Based Syst.*, vol. 300, Sep. 2024, Art. no. 112098, doi: 10.1016/j.knosys.2024.112098.
[23] A. Brodzicki, M. Piekarski, and J. Jaworek-Korjakowska, "The whale optimization algorithm approach for deep neural networks," *Sensors*, vol. 21, no. 23, p. 8003, Nov. 2021, doi: 10.3390/s21238003.
[24] B. A. Hassan, T. A. Rashid, A. M. Ahmed, S. M. Qader, J. Majidpour, M. H. Abdalla, N. Tayfor, H. K. Hamarashid, H. Sidqi, and K. A. Noori, "Equitable and fair performance evaluation of whale optimization algorithm," in *Handbook of Whale Optimization Algorithm*. Amsterdam, The Netherlands: Elsevier, 2024, pp. 157–168.
[25] M. T. Abdulkhaleq, T. A. Rashid, B. A. Hassan, A. Alsadoon, N. Bacanin, A. Chhabra, and S. Vimal, "Fitness dependent optimizer with neural networks for COVID-19 patients," *Comput. Methods Programs Biomed. Update*, vol. 3, Jan. 2023, Art. no. 100090, doi: 10.1016/j.cmpbup.2022.100090.
[26] O. Ronneberger, P. Fischer, and T. Brox, "U-Net: Convolutional networks for biomedical image segmentation," in *Proc. 18th Int. Conf. Med. Image Comput. Comput.-Assist. Intervent. (MICCAI)*, in Lecture Notes in Computer Science, vol. 9351, N. Navab, J. Hornegger, W. M. Wells, and A. F. Frangi, Eds. Cham, Switzerland: Springer, 2015, pp. 234–241.
[27] J. L. Wang, X. H. Qu, and Y. Zhao, "Design of lighting system in multi vision detection," *Electro-Optic Technol. Appl.*, vol. 24, no. 4, pp. 1–5, 2009.
[28] H. J. Liu, Y. N. Wang, and F. Duan, "Image capture in machine vision," *Comput. Inf. Technol.*, vol. 1, pp. 18–21, Jan. 2003.
[29] L. Nian, X. Pei, Z. Zhao, and X. Wang, "Review of optical designs for light-emitting diode packaging," *IEEE Trans. Compon., Packag., Manuf. Technol.*, vol. 9, no. 4, pp. 642–648, Apr. 2019.
[30] T. P. Nguyen, S. Choi, S.-J. Park, S. H. Park, and J. Yoon, "Inspecting method for defective casting products with convolutional neural network (CNN)," *Int. J. Precis. Eng. Manuf.-Green Technol.*, vol. 8, no. 2, pp. 583–594, Mar. 2021.
[31] Z. Ren, F. Fang, N. Yan, and Y. Wu, "State of the art in defect detection based on machine vision," *Int. J. Precis. Eng. Manuf.-Green Technol.*, vol. 9, no. 2, pp. 661–691, Mar. 2022.
[32] W.-C. Ma, S.-H. Chao, B.-Y. Chen, C.-F. Chang, M. Ouhyoung, and T. Nishita, "An efficient representation of complex materials for real-time rendering," in *Proc. ACM Symp. Virtual Reality Softw. Technol.*, Nov. 2004, pp. 150–153.
[33] H. Zhang, C. Zhang, C. Wang, and F. Xie, "A survey of non-destructive techniques used for inspection of bearing steel balls," *Measurement*, vol. 159, Jul. 2020, Art. no. 107773.
[34] B. T. Phong, "Illumination for computer generated pictures," *Commun. ACM*, vol. 18, no. 6, pp. 311–317, Jun. 1975.
[35] M. Szydłowski, B. Powałka, M. Matuszak, and P. Kochmański, "Machine vision micro-milling tool wear inspection by image reconstruction and light reflectance," *Precis. Eng.*, vol. 44, pp. 236–244, Apr. 2016.
[36] O. Russakovsky, J. Deng, H. Su, J. Krause, S. Satheesh, S. Ma, Z. Huang, A. Karpathy, A. Khosla, M. Bernstein, A. C. Berg, and L. Fei-Fei, "ImageNet large scale visual recognition challenge," *Int. J. Comput. Vis.*, vol. 115, no. 3, pp. 211–252, Dec. 2015.
[37] M. Everingham, L. Van Gool, C. K. I. Williams, J. Winn, and A. Zisserman, "The PASCAL visual object classes (VOC) challenge," *Int. J. Comput. Vis.*, vol. 88, no. 2, pp. 303–338, Jun. 2010.
[38] G. Karaduman and E. Akin, "A deep learning based method for detecting of wear on the current collector strips' surfaces of the pantograph in railways," *IEEE Access*, vol. 8, pp. 183799–183812, 2020, doi: 10.1109/ACCESS.2020.3029555.
[39] I. I. Medina, G. Arana, A. C. C. Atoche, J. J. E. López, J. V. Castillo, F. Avilés, and A. A. C. Atoche, "Adhesion testing system based on convolutional neural networks for quality inspection of flexible strain sensors," *IEEE Trans. Ind. Informat.*, vol. 20, no. 7, pp. 9235–9243, Jul. 2024.
[40] D. Weimer, S. Scholz, and J. Beyerer, "Design, automation and test of CNNs for rapid image recognition in optical quality control," *IEEE Trans. Ind. Informat.*, vol. 12, no. 3, pp. 1234–1243, Mar. 2016.
[41] X. Tao, D. Zhang, W. Ma, X. Liu, and D. Xu, "Automatic metallic surface defect detection and recognition with convolutional neural networks," *Appl. Sci.*, vol. 8, no. 9, p. 1575, Sep. 2018.
[42] J. Masci, U. Meier, D. Ciresan, J. Schmidhuber, and G. Fricout, "Steel defect classification with max-pooling convolutional neural networks," in *Proc. Int. Joint Conf. Neural Netw. (IJCNN)*, Jun. 2012, pp. 1–6.

MÜHENAD BILAL received the B.Sc. degree in general physics from the Philips University of Marburg, in 2014, the M.Sc. degree, in 2016, with a specialization in optics, focusing on the photoluminescence spectroscopy of organic solar cells. He is currently pursuing the Ph.D. degree with the Technical University of Ingolstadt. His bachelor's thesis was on III/V compound semiconductor materials. From 2017 to 2018, he was a Research Associate with the Laser Center Hannover, working on laser-induced damage and total scattering. Then, he was a Development Engineer of optical systems with Instrument Systems GmbH, until 2020. Since 2020, he has been a Research Associate with the Technical University of Ingolstadt. Since 2021, he has been the Project Manager and the Team Leader with WMH Herion Antriebstechnik GmbH, developing AI-based optical wear detection systems and intelligent business processes using machine learning approaches. He has invented patents in the field of physical science.

RANADHEER PODISHETTI was born in Hyderabad, India. He received the B.S. degree in mechanical engineering from Jawaharlal Nehru Technological University, Hyderabad. After his graduation, he joined the Amazon Development Center, Hyderabad, as a Data Analyst, where he worked for a year, analyzing large data sets to optimize user experience. Then, he moved to Wolnzach, Germany, to work as an AI Engineer with Linner GmbH, for two years, focusing on developing advanced machine learning models. Currently, he is a Research Assistant with Technische Hochschule Ingolstadt, Germany, where he is involved in cutting-edge research in medical imaging.

LEONID KOVAL received the B.Sc. and M.Sc. degrees in mechatronics from Technische Hochschule Ingolstadt, in 2015 and 2017, respectively.

He was a Scientific Research Assistant with Technische Hochschule Ingolstadt, in 2015, in parallel to his master's studies, and as a Development Engineer with Linner Elektronik GmbH, from 2017 to 2018. He has been a Scientific Research Assistant with Technische Hochschule Ingolstadt, since 2018. His research interests include image processing in end-of-line tests and deep neural networks for industrial applications.

MAHMOUD A. GAAFAR received the joint M.Sc. degree in physics from Joint Institute for Nuclear Research (JINR), Moscow, Russia, and Menoufia University, Egypt, in March 2012, and the Ph.D. degree from the Philipps-Universität Marburg, Marburg, Germany, in 2015, with a focus on the characterization and mode-locking of vertical-external-cavity surface-emitting lasers. From 2010 to 2012, he was with JINR. From 2016 to 2021, he was a Research Scientist with the Institute of Optical and Electronic Materials, Hamburg University of Technology, Hamburg, Germany. His current research interests include the development and implementation of concepts for dynamic control of light in integrated waveguide systems. He is a member of the Optical Society of America (OSA) and German Physical Society (DPG).

DANIEL GROSSMANN received the degree in mechanical engineering from the Technical University of Munich, specializing in information technology and automation engineering. He is currently a Professor of engineering informatics and data processing with Technische Hochschule Ingolstadt. Previously, he was a Research Area Coordinator with the ABB AG Research Center, Germany. In this role, he contributed to the strategic orientation of corporate research and led several working groups in international standardization. His research interests include IM, industry 4.0, cyber-physical systems, and the Industrial Internet of Things. For his doctorate at TU Munich in the field of device integration, he received the NAMUR Award, in 2008.

MARKUS BREGULLA received the Diploma Engineering degree in electronic equipment from TU Gleiwitz and the Dr.-Ing. degree from TU Munich, in 2002.

Since 2002, he has been with Technische Hochschule Ingolstadt, Germany, a full-time Professor of automation technology and engineering informatics. His research interests include industrial control systems, diagnostics of distributed complex automation systems, and design methods for industrial systems. He has experience in both academic and industrial research.